





Experimental investigation of turbulent flow over a sharp-crested circular cylindrical segment

Ali Shirinzad ^{*}, Sedem Kumahor , Amir Sagharichi , and Mark Francis Tachie 
Department of Mechanical Engineering, University of Manitoba, Winnipeg, Manitoba R3T 5V6, Canada



(Received 6 March 2023; accepted 10 July 2023; published 28 July 2023)

A circular cylindrical segment is a sharp-crested weir with a circular downstream curve profile. Overflow characteristics of circular cylindrical and circular-crested weirs have been studied extensively over the past century. Meanwhile, the available literature on the circular cylindrical segment is comparatively limited. Previous studies have often employed the potential flow theory to predict the mean velocities, pressure, and discharge coefficient, which may not be able to accurately predict the flow characteristics for a circular cylindrical segment. The aim of the present study is to experimentally investigate turbulent flows over circular cylindrical segments and to provide equations that can predict the mean velocities along the weir. Three upstream face angles $\alpha = 90^\circ$, 45° , and 30° , and three water depths over the crest $D_c/h = 0.7$, 0.4 , and 0.2 , were tested to simultaneously characterize the effects of both the upstream face angle and water depth. The instantaneous velocities were measured using a planar particle image velocimetry system in an open recirculating water channel. The results showed the presence of a recirculation bubble at the crest of the weir for all test conditions. The size of this recirculation zone decreases as the water depth or the upstream face angle decreases. At a far enough distance from the recirculation zone, the mean angular momentum varied linearly in the circumferential direction. Meanwhile, a rigid-body rotation region was detected near the free surface, which grows thicker in the circumferential direction.

DOI: [10.1103/PhysRevFluids.8.074605](https://doi.org/10.1103/PhysRevFluids.8.074605)

I. INTRODUCTION

A. Background

A weir is a small-scale dam built across a stream to regulate the flow of water or feed a diversion channel. Stream flows are allowed to pass over the top of a weir. However, for large-scale dams, overtopping may lead to potential failure, and consequently, the excess stream flows are released into the downstream riverbed through hydraulic structures known as spillways [1]. Weirs are categorized into four groups based on the crest shape, namely, long-crested, broad-crested, short-crested, and sharp-crested [2]. A weir with a thin width edge is termed sharp-crested, whereas one with appreciable width is called broad-crested [3].

Circular weirs are among the most common hydraulic structures that are used for discharge measurements, flow diversion, and regulating water levels [4–6]. These weirs are very convenient for designers due to their ability to efficiently pass floating debris, design simplicity compared to ogee-crested weirs, and relatively lower costs [7]. Geometrical differences investigated in previous studies are shown in Fig. 1.

^{*}Corresponding author: shirinza@myumanitoba.ca

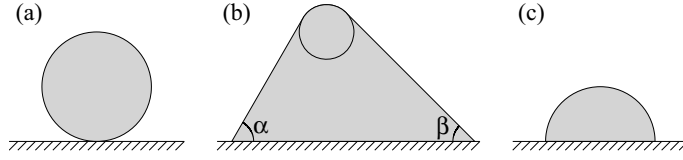


FIG. 1. Schematics of the previously studied circular geometries: (a) circular cylinder, (b) circular-crested weir, and (c) semicircular cylinder.

The simplest form of circular weirs is a circular cylinder set perpendicular to the oncoming flow. A circular-crested weir is an overflow structure with a circular crest positioned tangentially to an upstream and a downstream face of angle α and β , respectively. Semicircular cylindrical weirs consist of half of a circular cylinder positioned perpendicular to the flow direction and were developed in the 1990s [8].

The first experimental study on circular weirs is attributed to Koch and Carstanjen [9]. Ever since, the effects of a wide range of flow parameters, such as surface tension, viscosity, and streamline curvature, on the hydraulic characteristics of circular weirs have been studied extensively [4,10–14], where it was shown that the discharge coefficient is a function of upstream head to crest radius ratio. Chanson and Montes [15] conducted experiments on the effects of geometrical parameters, such as circular cylinder radius and weir height, as well as upstream conditions on the overflow characteristics of circular weirs. Their results revealed that the upstream hydraulic conditions significantly affect the overflow properties. Ramamurthy and Vo [13] experimentally investigated the effects of both upstream and downstream face angle on the discharge coefficient of circular-crested weirs, where it was shown that changing the upstream face slope did not alter the discharge coefficient; however, increasing the downstream face slope apparently increased the discharge coefficient.

The flow around circular weirs is often considered to be inviscid and irrotational, and consequently, the potential flow theory is employed to characterize the flow [16–19]. For instance, Ramamurthy and Vo [17] used the expression of Dressler [16] for the velocity profile of a shallow irrotational flow over a curved bed to predict the velocity distribution over circular weirs. Previous studies show that the results obtained from the potential flow theory often agree well with the reported experimental values [17,18,20]. It should be noted that the motion of the free surface can only be modeled by the potential flow theory when the free surface undergoes a small deformation, and for a highly deformed free surface with turbulence, the inviscid model is no longer valid [8].

B. Objectives

Despite the geometrical similarities between the circular-crested weirs and the circular cylindrical segment, circular-crested weirs are classified as narrow-crested [21] or short-crested weirs [22], whereas the circular cylindrical segment is considered sharp-crested. From the discussion in Sec. IA, it is clear that a considerable number of analytical, experimental, and numerical studies have already been conducted on circular cylindrical and circular-crested weirs. In comparison, the available literature on the overflow characteristics of a circular cylindrical segment is very limited. Therefore, the objectives of this paper are as follows:

(i) Investigate the effects of both the upstream face angle α and water depth at the crest D_c on the flow properties over circular cylindrical segments.

(ii) Propose physical models to characterize the mean velocities along the weir.

The remainder of the paper is organized as follows. A description of the flow and the adopted nomenclature is presented in Sec. II. The experimental setup, methodology, and post-processing procedure are described in Sec. III. The main results and discussion are presented in Sec. IV and the major findings and conclusions are summarized in Sec. V.

II. DESCRIPTION OF THE FLOW

Consider the flow over a circular cylindrical segment, as sketched in Fig. 2. Geometrical and flow parameters upstream and at the leading edge (crest) are denoted by subscripts ‘*o*’ and ‘*c*’, respectively. All angles are in radians unless when explicitly specified in degrees ($^{\circ}$).

Polar-cylindrical (r, θ, z), curvilinear (n, s), and Cartesian (x, y) coordinate systems are adopted, where the polar-cylindrical and curvilinear coordinate systems are related through Eqs. (1a) and (1b):

$$n = r - r_c, \quad (1a)$$

$$s = r_c(\theta - \theta_c). \quad (1b)$$

The circular cylindrical segment has a height of h , with the leading edge being at $\theta = \theta_c$, and an upstream face angle of α . The velocities in the Cartesian coordinate system are denoted by u and v in the x and y coordinate directions, respectively. The velocity components in the polar-cylindrical coordinate system are denoted by u_θ , v_r , and w_z in the r , θ , and z coordinate directions, respectively. Velocities in the curvilinear coordinate system in the n and s coordinate directions are the same as the velocities in the r and θ coordinate directions in the polar-cylindrical coordinate system. Following Reynolds [23], the fluctuating velocities are designated by the prime symbol, while statistical moments of fluctuating quantities are denoted using an overline. All of the mean quantities are represented using a capital letter.

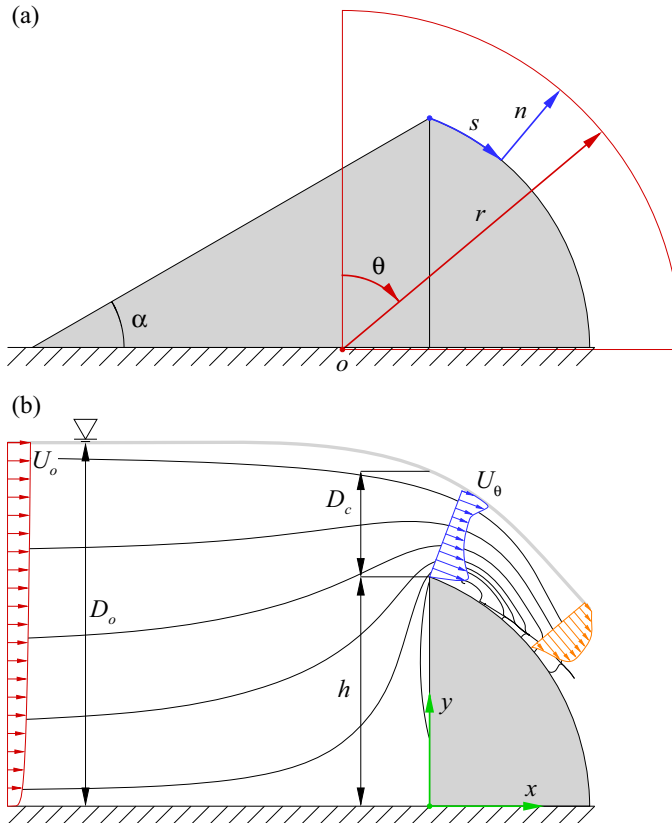


FIG. 2. A schematic showing (a) a circular cylindrical segment with an upstream face angle of α and (b) the adopted nomenclature.

Water flows steadily through a rectangular open channel and produces a velocity profile with a free-stream velocity of U_o . The presence of the weir causes the velocity profile to deform significantly at the crest, which is schematically shown by U_θ in Fig. 2. As the flow passes over the weir, the free surface remains smooth and nonaerated, and the streamlines strongly adhere to the weir surface, a phenomenon referred to as the Coanda effect [7]. At the leading edge, flow separation occurs due to the sharp crest geometry and the inclined surface of the weir. The flow eventually reattaches to the weir surface, forming a recirculation bubble near the leading edge before leaving the circular cylindrical segment.

III. EXPERIMENTAL PROCEDURE

A. Test section and test cases

The experiments were conducted at the Turbulence and Hydraulic Engineering Laboratory (THEL), University of Manitoba, in an open recirculating water channel with a working section 6.00 m long, 0.45 m high, and 0.60 m wide. The bottom and sidewalls of the test section were fabricated from 31.8 mm thick transparent Abrasion-Resistant[®] acrylic plates to facilitate optical access from all sides. The flow in the channel was driven by a 30 kW variable-speed drive motor capable of producing a maximum discharge of 0.566 m³/s. The speed of the pump was controlled using a variable frequency drive assembly that could vary the oncoming velocity from 0.03 m/s to 2.00 m/s. A flow conditioning unit, consisting of a series of perforated plates, hexagonal honeycombs, mesh screens, and a 4.88:1 converging section, was installed upstream of the test section to minimize the turbulence and homogenize the oncoming flow entering the test section. The water exiting the test section was redirected to the return pipe through a turning vane system for flow recirculation.

A circular cylindrical segment of height $h = 0.15$ m, upstream face angle $\alpha = 90^\circ$, crest angle $\theta_c = 20.6^\circ$, and span-wise width of 0.60 m was installed on the channel floor, 2.50 m downstream of the entrance to the test section. Two additional upstream face angles $\alpha = 45^\circ$ and 30° were examined by installing 45° and 30° wedges immediately upstream of the weir. The wedges were 0.15 m high and spanned the entire width of the channel. All physical models were fabricated from smooth acrylic plates in the Machine Shop at Price Faculty of Engineering, University of Manitoba. A sketch showing the examined geometries is presented in Fig. 3.

Three water depths over the crest, including $D_c/h = 0.7$, 0.4, and 0.2, were investigated for each upstream face angle. The water depth over the crest was set to the desired level by keeping the oncoming velocity constant, monitoring the free surface, and draining the surplus water from the channel. The room temperature was regulated at 20 °C, leading to a kinematic viscosity of $\nu = 1.0 \times 10^{-6}$ m²/s for water. Table I provides a summary of the pertinent test parameters and dimensionless numbers. The examined Reynolds numbers are large enough to establish turbulent flow conditions.

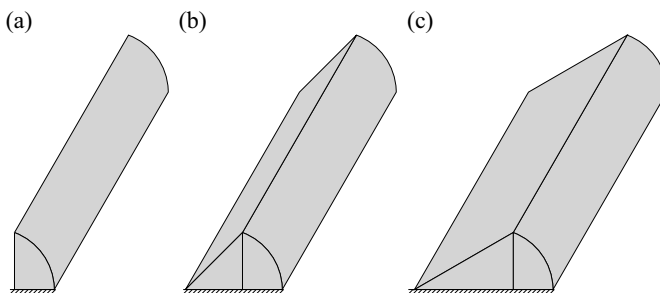


FIG. 3. A schematic showing the tested weirs: (a) $\alpha = 90^\circ$, (b) $\alpha = 45^\circ$, and (c) $\alpha = 30^\circ$.

TABLE I. Summary of the flow parameters.

α	D_o/h	D_c/h	U_o (m/s)	U_c (m/s) ^a	$Re_h = U_o h/\nu$	$Fr_o = U_o/\sqrt{gD_o}$ ^b	$Fr_c = U_c/\sqrt{gD_c}$ ^b
90°	1.63	0.70	0.308	1.476	46200	0.199	1.453
	1.40	0.45	0.162	1.175	24300	0.113	1.444
	1.20	0.25	0.069	0.755	10350	0.052	1.225
45°	1.68	0.71	0.308	1.488	46200	0.196	1.456
	1.42	0.42	0.162	1.179	24300	0.112	1.500
	1.21	0.20	0.069	0.761	10350	0.052	1.403
30°	1.68	0.67	0.308	1.457	46200	0.196	1.467
	1.46	0.43	0.162	1.239	24300	0.111	1.558
	1.22	0.21	0.069	0.756	10350	0.051	1.360

^aMaximum velocity is reported at the crest.

^b $g = 9.81 \text{ m/s}^2$ was used to evaluate the Froude numbers.

Furthermore, $Fr_o < 1$ and $Fr_c > 1$ for all test cases, indicating the transitions of the flow from subcritical to supercritical regime.

B. Particle image velocimetry (PIV) system

A two-component particle image velocimetry (PIV) system was employed to measure the velocity fields at the span-wise centerline. Here, parameters associated with the particles and the working fluid are designated by subscripts ‘ p ’ and ‘ f ’, respectively. The flow was seeded with silver coated hollow glass spheres, which had a diameter of $d_p = 10 \mu\text{m}$ and a specific gravity of 1.4. The flow field was illuminated by a diode-pumped dual-cavity high-speed Neodymium-doped yttrium lithium fluoride (Nd:YLF) laser (DM30-527DH, Photonics Industries International, Inc.). Each cavity was capable of emitting green light up to a maximum pulse energy of 30 mJ/pulse at a wavelength of 527 nm and an operation frequency of 1000 Hz. The thickness of the laser light sheet was approximately 1.5 mm. Two high-speed 12-bit complementary metal oxide semiconductor cameras (CMOS), positioned side-by-side and fitted with Nikon 60 mm lenses, were operated at a resolution of 2560 pixels \times 1600 pixels to simultaneously capture the light scattered by the illuminated seeding particles within the fields of view. Both fields of view were 195.8 mm long and 313.7 mm high, and overlapped by 10.0 mm in the stream-wise direction. A schematic showing the test section and the PIV arrangements is provided in Fig. 4.

In the operation of the PIV, the ability of the particles to faithfully follow the fluid motions must be critically evaluated. Following Raffel *et al.* [24], the slip velocity of particles was estimated from

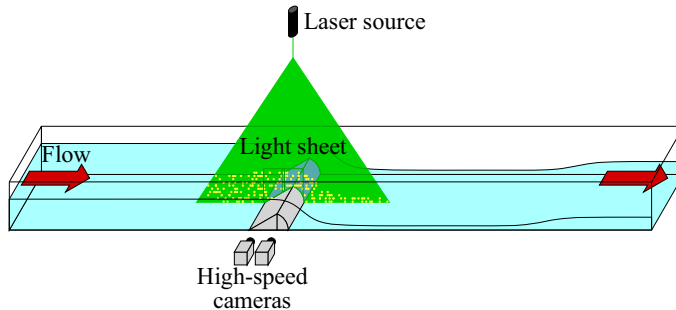


FIG. 4. A schematic representing the test section, PIV arrangements, and the fields of view.

Eq. (2):

$$u_s = \frac{d_p^2(\rho_p - \rho_f)g}{18\rho_f\nu}. \quad (2)$$

In Eq. (2), ρ and g denote the density and the gravitational acceleration, respectively. The calculated slip velocity was 2.18×10^{-5} m/s, which was four orders of magnitude lower than the free-stream velocity. The relaxation time $\tau_p = u_s/g$ was estimated to evaluate the response time of the seeding particles to sudden motions in flow velocity. The PIV system was operated in time-resolved mode at a sampling frequency of 800 Hz to evaluate the Taylor microtime scale τ_f , which is the smallest temporal scale that could be measured in the present study. The Stokes number $Sk = \tau_p/\tau_f$, which is a measure of the particle response time relative to the characteristic time scale of the small eddies, was 4.53×10^{-5} for $\alpha = 90^\circ$ and $D_c/h = 0.7$ test case, which is orders of magnitude smaller than the threshold value of 0.05 proposed by Samimy and Lele [25]. As such, the seeding particles followed the fluid motions well, and their instantaneous velocities were an accurate representation of the instantaneous local fluid velocities.

The PIV system was operated in the double-frame mode at a sampling frequency of 3 Hz to obtain statistically independent samples. For each test case, a total number of 12 000 images were recorded, resulting in a total sampling time of 2000 seconds. Data acquisition, image processing, and vector calculations were controlled using commercial software DaVis[®] (version 10.0.5, supplied by LaVision Inc.). The velocity vectors were calculated using a GPU-accelerated multipass cross-correlation algorithm, using an initial interrogation area of 64 pixels \times 64 pixels with 50 % overlap, and an interrogation area of 16 pixels \times 16 pixels with 75 % overlap during the four final passes. The resulting vector spacing was 0.48 mm, which corresponds to 0.0032 h .

C. Post-processing and uncertainty quantification

Commercial software Matlab[®] was used for data post-processing and calculating the time-averaged velocities and higher statistical moments. For each camera, velocity measurements were performed with respect to a local Cartesian coordinate system. The two fields of view were transformed and joined together to form a united domain with a new Cartesian coordinate system, as was shown in Fig. 2. All of the redundant data point within the geometries and above the free surface were identified and blanked using the algorithm developed by Hormann and Agathos [26]. A set of expressions used for obtaining the mean velocities and Reynolds stresses in the polar-cylindrical coordinate system is provided in Appendix. Measurement uncertainty in the mean velocities and Reynolds stresses were evaluated within 95 % confidence level following Sciacchitano and Wieneke [27] and Bendat and Piersol [28]. For $\alpha = 90^\circ$ and $D_c/h = 0.7$ test case at a selected location above the crest $(x, y) = (0, h + D_c/2)$ the uncertainty values for the mean velocities and Reynolds stresses were 0.06 % and 2.92 %, respectively.

Data analysis and visualization were accomplished using commercial software Tecplot 360 EX[®] and Origin[®]. All plots presented henceforth are normalized using the oncoming velocity U_o and the height of the weir model h .

IV. RESULTS AND DISCUSSION

In this section, contour plots as well as both radial and circumferential one-dimensional profiles are presented to provide detailed measurements of flow characteristics. Radial one-dimensional profiles of various parameters, including the mean span-wise vorticity, the mean angular momentum, and correlation coefficient, were evaluated at eleven successive locations, starting at $s/h = 0.00$ and ending at $s/h = 0.50$ with an increment of 0.05 h , while the range of the normal axis was limited to $0 \leq n/h \leq D_c/h$. The circumferential profiles were plotted at several radial locations, depending on the water depth. For each water depth, a color palette is presented on the right-hand side of the plots.

A. Mean span-wise vorticity

The mean span-wise vorticity is evaluated to investigate the rotation of fluid elements. For a steady incompressible flow, the Reynolds averaged continuity equation and the mean span-wise vorticity in polar cylindrical coordinate system are given by Eqs. (3a) and (3b):

$$\frac{\partial U_\theta}{r\partial\theta} + \frac{\partial rV_r}{r\partial r} + \frac{\partial W_z}{\partial z} = 0, \quad (3a)$$

$$\Omega_z = \frac{1}{r} \left(\frac{\partial rU_\theta}{\partial r} - \frac{\partial V_r}{\partial\theta} \right). \quad (3b)$$

To minimize computational errors, however, $\partial W_z/\partial z$ and Ω_z were directly calculated from the mean velocities in the Cartesian coordinate system using Eqs. (4a) and (4b), respectively,

$$\frac{\partial W_z}{\partial z} = \frac{\partial U}{\partial x} + \frac{\partial V}{\partial y}, \quad (4a)$$

$$\Omega_z = \frac{\partial U}{\partial y} - \frac{\partial V}{\partial x}. \quad (4b)$$

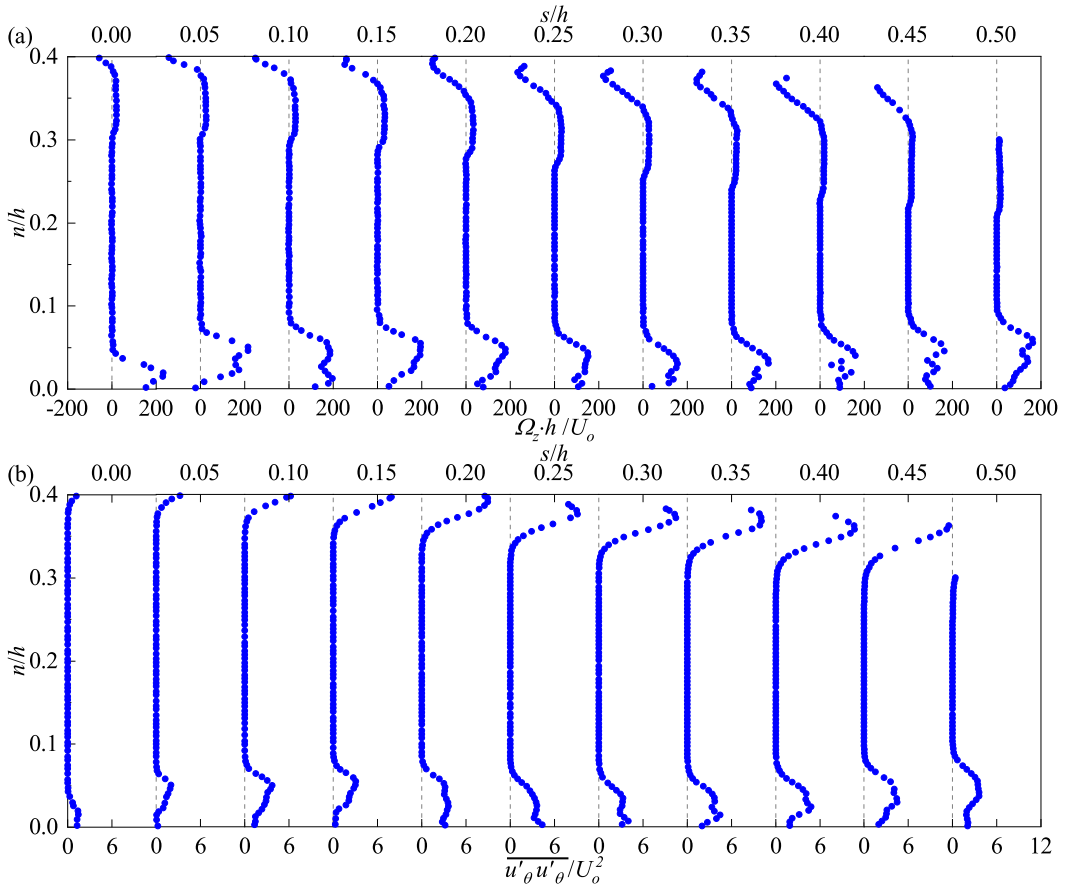


FIG. 5. Circumferential evolution of the radial profiles of the normalized mean span-wise vorticity and stream-wise Reynolds stress for $\alpha = 30^\circ$ at $D_c/h = 0.4$.

Figure 5 shows the circumferential evolution of the radial profiles of the normalized mean span-wise vorticity and the stream-wise Reynolds stress for $\alpha = 30^\circ$ at $D_c/h = 0.4$. An essential feature of turbulent flows is that they are rotational. Elevated regions of the mean span-wise vorticity are observed along the weir and the free surface, where the flow was highly turbulent. The normalized Reynolds stresses in these two regions were at most an order of 10. Two additional regions are also identified on Fig. 5:

(i) A region close to the free surface where the mean span-wise vorticity is invariant in the radial direction. Upon further investigations, it was observed that $\partial W_z/\partial z$ is nearly zero in this region, and consequently, the flow may be considered to be in rigid-body rotation. The normalized stream-wise Reynolds stress in this region was at most an order of 10^{-2} .

(ii) An irrotational region extending between the edge of the turbulent region along the weir and the rigid-body rotation region. In this region, $\partial W_z/\partial z$ was negligible and the normalized stream-wise Reynolds stress was an order of 10^{-3} .

A clear observation from Fig. 5(a) is that, in the rigid-body rotation region, the mean span-wise vorticity greatly varies in the circumferential direction. To further evaluate the flow characteristics upstream of the weir, contour plots of the normalized mean span-wise vorticity and stream-wise Reynolds stress for $\alpha = 30^\circ$ and $\alpha = 90^\circ$ at $D_c/h = 0.4$ are presented in Fig. 6. Both Figs. 5(a) and

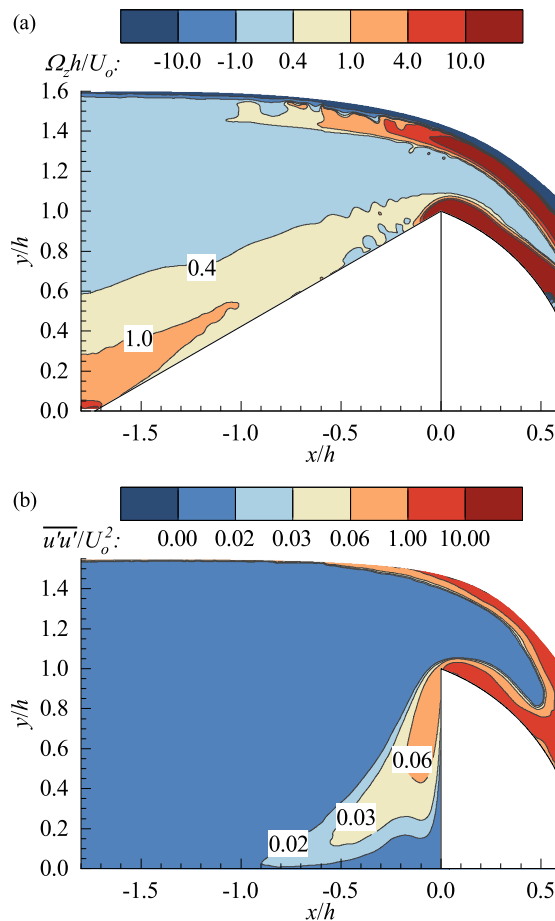


FIG. 6. Contour plots of (a) normalized mean span-wise vorticity and (b) normalized stream-wise Reynolds stress for $\alpha = 30^\circ$ and $\alpha = 90^\circ$ at $D_c/h = 0.4$ test cases.

TABLE II. Summary of the entrance parameters.

α	D_c/h	θ_e^a	s_e/h^b
90°	0.4	47.1°	0.50
90°	0.2	35.7°	0.28
45°	0.2	42.8°	0.42
30°	0.2	43.9°	0.44

^aThe entrance angle for the test cases not reported here was either out of the field of view or nonexistent.

^bThe entrance length was obtained from Eq. (1b).

6(a) clearly indicate that the thickness of the rigid-body rotation region grows as the flow develops in the circumferential direction. An interesting observation from Fig. 6(a) is that the onset of the rigid-body motion extends to $\theta = 0$. In fact, for several test cases, even at $\theta = 0$, the mean span-wise vorticity is still nonzero.

Figure 6(b) shows high levels of stream-wise Reynolds stress upstream of the weir, which is a consequence of the upstream flow separation due to the adverse pressure gradient specific to the $\alpha = 90^\circ$ test cases. From Fig. 6(b) it can be seen that, over the weir, the turbulent regions are initially confined to thin layers near the weir and free surface. However, when the flow develops sufficiently in the circumferential direction, the turbulent regions eventually fill the entire cross-sectional area. Consequently, a developing region may be defined in a similar manner to other types of weirs and spillways. For example, for a chute spillway, the developing flow region consists of a turbulent boundary layer next to the above ideal-fluid flow region [29].

For this particular weir, the developing region consists of the irrotational region next to the above rigid-body rotation region in the middle, surrounded by the outer turbulent regions along the weir and the free surface. Table II compares the entrance parameters for several test cases.

The entrance parameters are denoted by subscript ‘e’. The entrance angle θ_e and the entrance length s_e strongly depend on the water depth; nonetheless, they are not significantly affected by the upstream face angle. Overall, the entrance length decreases as the water depth decreases and increases as the upstream face angle decreases.

Circumferential profiles of the normalized mean span-wise vorticity in the rigid-body rotation region for all test cases are presented in Fig. 7. Note that a polar line may span multiple flow regions and that the data points in other regions are not shown. A common feature of the profiles shown in Fig. 7 is that the mean span-wise vorticity increases to its maximum at $\theta = \theta_a$ before decreasing. Evidently, the value of θ_a decreases as the water depth decreases. Figure 7 clearly indicates that the circumferential profiles are strongly dependent on the water depth. Variations in the upstream face angle, on the other hand, do not alter the profiles significantly.

B. Mean angular momentum

The mean angular momentum is defined by Eq. (5) as

$$L = rU_\theta. \quad (5)$$

Based on the discussion in Sec. IV A, the flow is irrotational and $\partial W_z / \partial z = 0$. Rearranging Eqs. (3a) and (3b), we obtain

$$\frac{\partial W_z}{\partial z} = 0 \Rightarrow \frac{1}{r^2} \frac{\partial^2 r U_\theta}{\partial \theta^2} = -\frac{\partial^2 r V_r}{r \partial \theta \partial r}, \quad (6a)$$

$$\Omega_z = 0 \Rightarrow \frac{1}{r} \frac{\partial}{\partial r} \left(r \frac{\partial r U_\theta}{\partial r} \right) = \frac{\partial^2 r V_r}{r \partial r \partial \theta}. \quad (6b)$$

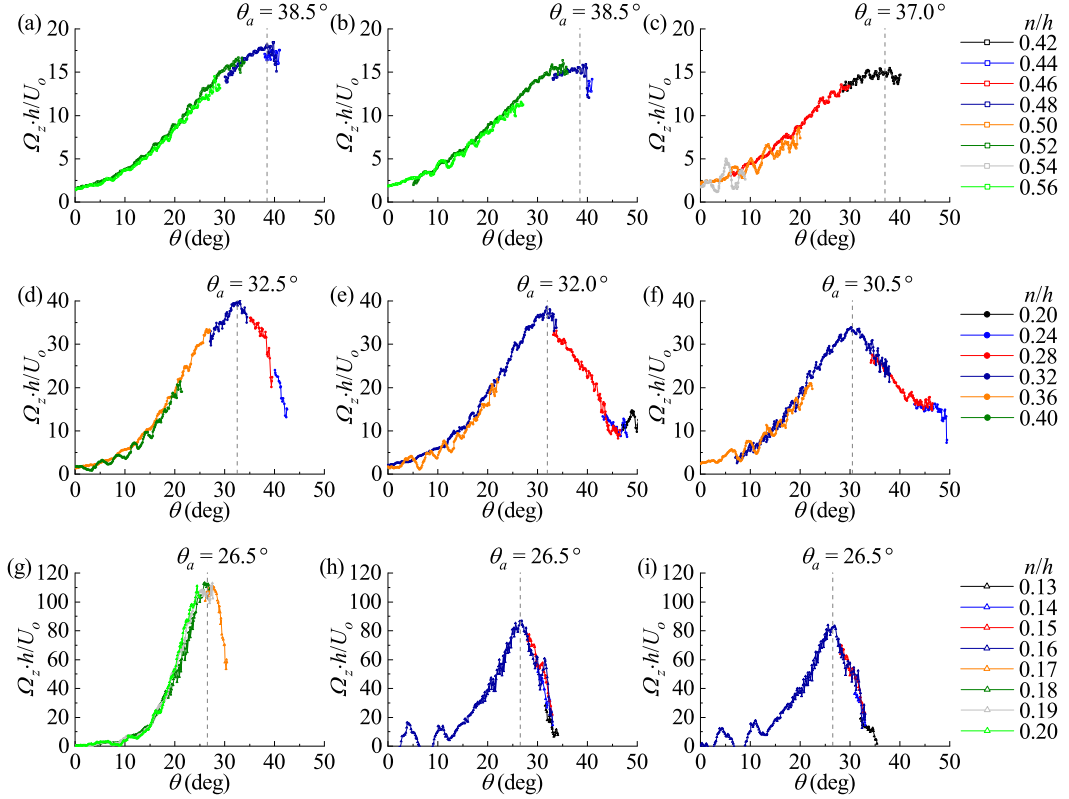


FIG. 7. Circumferential profiles of the normalized mean span-wise vorticity in the rigid-body rotation region: (a) $\alpha = 90^\circ$ and $D_c/h = 0.7$, (b) $\alpha = 45^\circ$ and $D_c/h = 0.7$, (c) $\alpha = 30^\circ$ and $D_c/h = 0.7$, (d) $\alpha = 90^\circ$ and $D_c/h = 0.4$, (e) $\alpha = 45^\circ$ and $D_c/h = 0.4$, (f) $\alpha = 30^\circ$ and $D_c/h = 0.4$, (g) $\alpha = 90^\circ$ and $D_c/h = 0.2$, (h) $\alpha = 45^\circ$ and $D_c/h = 0.2$, and (i) $\alpha = 30^\circ$ and $D_c/h = 0.2$.

Now applying Clairaut's theorem (Symmetry of second partial derivatives) to Eqs. (6a) and (6b), we eliminate the mean radial velocity to arrive at the governing relations for the mean angular momentum

$$\nabla^2 r U_\theta = 0, \quad (7a)$$

$$r \frac{\partial}{\partial r} \left(r \frac{\partial r U_\theta}{\partial r} \right) = - \frac{\partial^2 r U_\theta}{\partial \theta^2}. \quad (7b)$$

When the mean angular momentum is specified, the mean radial velocity may easily be obtained by integrating and simultaneously solving Eqs. (8a) and (8b) as follows:

$$\frac{\partial V_r}{\partial \theta} = \frac{\partial r U_\theta}{\partial r}, \quad (8a)$$

$$r \frac{\partial r V_r}{\partial r} = - \frac{\partial r U_\theta}{\partial \theta}. \quad (8b)$$

The circumferential evolution of the radial profiles of the normalized mean angular momentum for $\alpha = 30^\circ$ at $D_c/h = 0.4$ is presented in Fig. 8. Negative values of the mean angular momentum, marked by red in Fig. 8, are observed near the leading edge due to the presence of the recirculation bubble. Furthermore, the angular momentum continuously increases in the circumferential direction within the developing region.

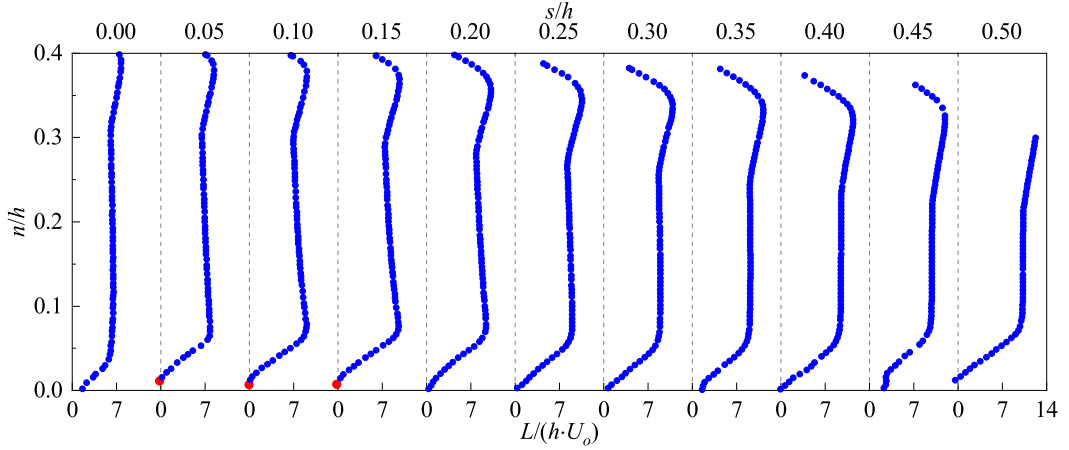


FIG. 8. Circumferential evolution of the radial profiles of the normalized mean angular momentum for $\alpha = 30^\circ$ at $D_c/h = 0.4$.

It is well known that the mean angular momentum is invariant in the radial direction for flow around a rotating circular cylinder due to axial symmetry. The present study shows that, even in the absence of axial symmetry, the radial invariance of the mean angular momentum may hold under certain conditions. As observed from Fig. 8, for $\alpha = 30^\circ$ at $D_c/h = 0.4$ test case, the mean angular momentum is almost invariant in the radial direction within the irrotational region after the reattachment of the flow (corresponding to profiles at $s/h \geq 0.30$ on Fig. 8), that is

$$rU_\theta = L_1(\theta). \quad (9)$$

Substituting Eq. (9) in Eq. (7b) gives rise to

$$\frac{d^2 L_1}{d\theta^2} = 0 \Rightarrow L_1(\theta) = A_1 \theta + B_1. \quad (10)$$

The mean circumferential velocity immediately follows from Eq. (9) while the mean radial velocity may easily be obtained by substituting Eq. (10) in Eqs. (8a) and (8b):

$$U_\theta = \frac{L_1(\theta)}{r} = \frac{A_1 \theta + B_1}{r}, \quad (11a)$$

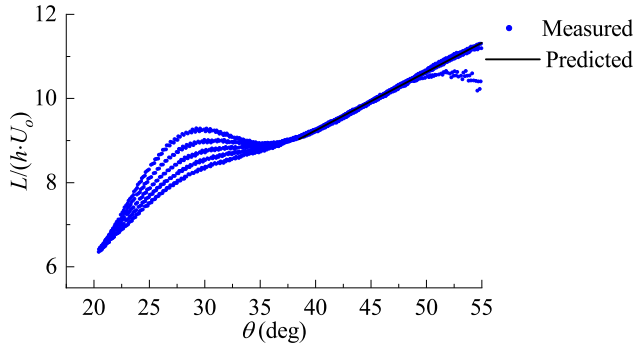
$$V_r = \frac{-A_1 \ln(r) + C_1}{r}. \quad (11b)$$

We can confirm Eq. (10) by examining whether the mean angular momentum varies linearly in the circumferential direction. Equation (10) was fitted to the experimental data of $\alpha = 30^\circ$ at $D_c/h = 0.4$ within $38.5^\circ < \theta < 55.0^\circ$, where a coefficient of determination of 0.997 was reached, indicating good agreement between the measured and predicted values. The obtained fitting parameters are summarized as

$$\frac{\widehat{L}_1}{h \cdot U_o} = \widehat{A}_1 \theta + \widehat{B}_1, \quad \widehat{A}_1 = 0.1388, \quad \widehat{B}_1 = 3.6893. \quad (12)$$

Figure 9 shows the plot of Eq. (10) fitted values superimposed on the measured data at $n/h = 0.10, 0.12, 0.14, 0.16,$ and 0.18 .

Circumferential profiles of the normalized mean angular momentum in the irrotational region for all test cases are shown in Fig. 10. As expected, the mean angular momentum is nonlinear above the recirculation bubble. Still, the profiles almost collapse on the same curve and vary linearly after the reattachment of the flow for several test cases. Note that for all $D_c/h = 0.7$ test cases, the


 FIG. 9. Plot of the predicted and measured $L/(h \cdot U_o)$ for $\alpha = 30^\circ$ at $D_c/h = 0.4$.

recirculation bubble is very large and spans the entire field of view. For several test cases, the linear profiles are followed by a sudden drop in the mean angular momentum, where a section of the polar line lies in the turbulent regions. This sudden drop in the mean angular momentum could be used to determine the entrance angle.

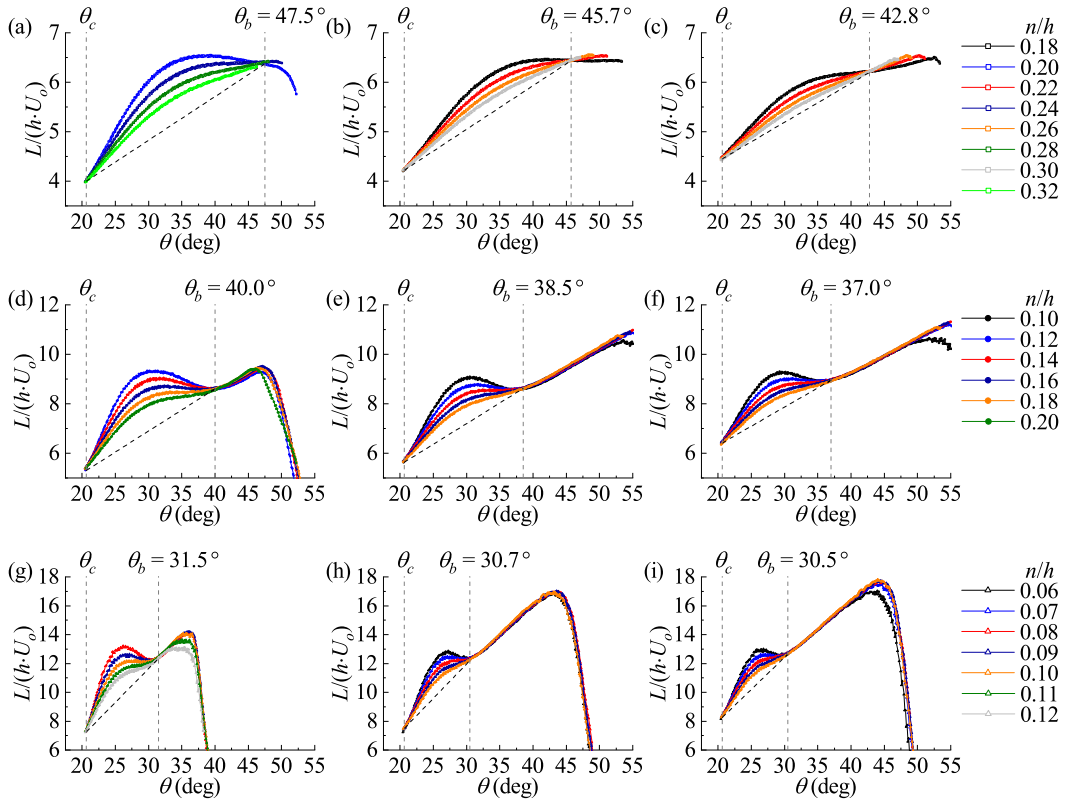


FIG. 10. Circumferential profiles of the normalized mean angular momentum in the irrotational region: (a) $\alpha = 90^\circ$ and $D_c/h = 0.7$, (b) $\alpha = 45^\circ$ and $D_c/h = 0.7$, (c) $\alpha = 30^\circ$ and $D_c/h = 0.7$, (d) $\alpha = 90^\circ$ and $D_c/h = 0.4$, (e) $\alpha = 45^\circ$ and $D_c/h = 0.4$, (f) $\alpha = 30^\circ$ and $D_c/h = 0.4$, (g) $\alpha = 90^\circ$ and $D_c/h = 0.2$, (h) $\alpha = 45^\circ$ and $D_c/h = 0.2$, and (i) $\alpha = 30^\circ$ and $D_c/h = 0.2$.

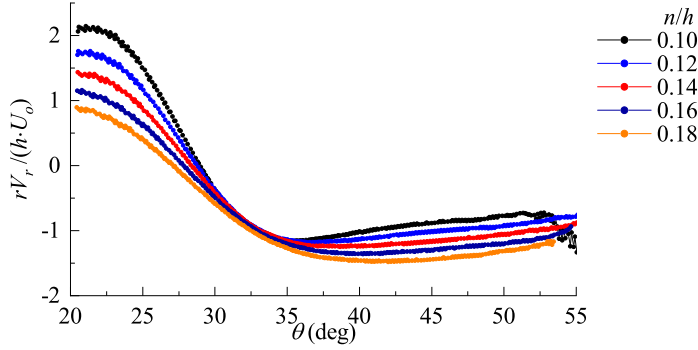


FIG. 11. Circumferential profiles of the normalized mean radial velocity in the irrotational region for $\alpha = 30^\circ$ at $D_c/h = 0.4$.

As a final remark on Eqs. (11a) and (11b), we emphasize that, even after the reattachment of the flow, $\partial rU_\theta/\partial r$ or equivalently $\partial V_r/\partial\theta$, may not be exactly equal to zero. Circumferential profiles of the normalized mean radial velocity are better suited to evaluate $\partial V_r/\partial\theta$. A set of such profiles for $\alpha = 30^\circ$ at $D_c/h = 0.4$ are provided in Fig. 11.

From Fig. 11, it is evident that $\partial rV_r/\partial\theta$ is apparently invariant in the circumferential direction within the linear range of the angular momentum. To further improve the predictions of the mean velocities, one may consider a linear model for the mean angular momentum

$$\frac{\partial L_2}{\partial\theta} = f(r). \quad (13)$$

Equation (13) asserts that the angular momentum profiles, although still varying linearly, do not necessarily collapse on the same line. Unlike Eq. (9), Eq. (13) is only a mathematical model based on experimental observations. Now solving Eqs. (13) and (7b) simultaneously, we obtain

$$r \frac{\partial}{\partial r} \left(r \frac{\partial L_2}{\partial r} \right) = 0 \Rightarrow L_2 = g(\theta) \ln(r) + h(\theta), \quad (14a)$$

$$\frac{\partial L_2}{\partial\theta} = f(r) \Rightarrow \frac{dg}{d\theta} \ln(r) + \frac{dh}{d\theta} = f(r). \quad (14b)$$

The left-hand side of Eq. (14b) cannot depend on θ , and consequently, $g(\theta)$ and $h(\theta)$ must be linear functions

$$g(\theta) = D_2\theta + E_2, \quad (15a)$$

$$h(\theta) = A_2\theta + B_2. \quad (15b)$$

Now, substituting Eqs. (15a) and (15b) in Eq. (14a), it follows that

$$L_2 = A_2\theta + B_2 + \ln r(D_2\theta + E_2). \quad (16)$$

Finally, Eqs. (5), (8a), and (8b) together with Eq. (16) give the distribution of the mean velocities

$$U_\theta = \frac{A_2\theta + B_2}{r} + \frac{\ln r}{r}(D_2\theta + E_2), \quad (17a)$$

$$V_r = \frac{-A_2 \ln r + C_2}{r} + \frac{D_2}{2} \left(\frac{\theta^2 - \ln^2 r}{r} \right) + E_2 \frac{\theta}{r}. \quad (17b)$$

Compared to Eq. (10), Eq. (16) allows for more flexibility for data fitting due to the extra logarithmic term. It should be noted that D_2 must be zero for the mean radial velocity to vary linearly in the circumferential direction. In such a case, the value of E_2 may be determined by calculating the

slopes of the circumferential profiles shown in Fig. 11. If E_2 is also set to zero, then Eqs. (17a) and (17b) simply reduce to Eqs. (11a) and (11b), respectively.

We now switch attention to the variations of the mean angular momentum above the recirculation bubble. The size of the recirculation bubble depends on several parameters, including the water depth, upstream face angle, and the wall inclination at the crest (θ_c). In the present study, the wall inclination at the crest was kept constant; nonetheless, the effects of varying wall inclination on the size of the recirculation bubble may be found in the previous studies [30]. The findings of the present study revealed that the size of the recirculation bubble decreases as the water depth decreases. The trajectory of the streamlines at the leading-edge significantly depends on the upstream face angle, and consequently, the size of the recirculation bubble decreases as the upstream face angle decreases.

From Fig. 10, it is evident that the mean angular momentum is a constant at the crest irrespective of the water depth and upstream face angle. Furthermore, for all test cases, the profiles diverge as the flow evolves over the recirculation bubble before eventually intersecting at a second location, denoted by θ_b . Henceforth, all parameters at this point are denoted by ‘ b ’ subscript. The value of θ_b decreases as the water depth decreases. The upstream face angle, on the other hand, does not significantly affect the value of θ_b . These experimental observations imply that the mean angular momentum is characterized by the characteristic angle $\varpi = \theta_b - \theta_c$ above the recirculation bubble, even though this is not evident from the geometrical constraints.

The line connecting the angular momentum intersection points (θ_c, L_c) and (θ_b, L_b) , as shown for all test cases in Fig. 10, is given by Eq. (18)

$$\Lambda(\theta) = A\theta + B, \quad A = \frac{L_b - L_c}{\theta_b - \theta_c}, \quad B = \frac{\theta_b L_c - \theta_c L_b}{\theta_b - \theta_c}. \quad (18)$$

An important observation from Fig. 10 is that the difference between the mean angular momentum circumferential profiles and $\Lambda(\theta)/(h \cdot U_o)$ decreases as the normal distance from the wall increases. In fact, for large enough values of n/h , the circumferential profiles almost collapse on the connecting line. To exclude the effects of recirculation bubble on the mean angular momentum, the angular momentum residual is defined by Eq. (19)

$$\Gamma(r, \theta) = L(r, \theta) - \Lambda(\theta). \quad (19)$$

The presence of a characteristic angle and the background linear angular momentum allow us to solve Eq. (7b) using the separation of variables technique. Another classical flow problem where such analysis are applied is the transient Couette flow [31]. Substituting Eq. (19) in Eq. (7b), we have

$$r \frac{\partial}{\partial r} \left(r \frac{\partial \Gamma}{\partial r} \right) = - \frac{\partial^2 \Gamma}{\partial \theta^2}. \quad (20)$$

Applying separation of variables to Eq. (20) yields

$$\Gamma(r, \theta) = \sum_n R_n(r) \Theta_n(\theta), \quad (21a)$$

$$\frac{r \frac{d}{dr} \left(r \frac{dR_n}{dr} \right)}{R_n} = - \frac{\frac{d^2 \Theta_n}{d\theta^2}}{\Theta_n} = \lambda_n^2. \quad (21b)$$

Therefore, $\Theta_n(\theta)$ must satisfy the second order linear differential equation described by Eq. (22a) and is a sine function as shown in Eq. (22b):

$$\frac{d^2 \Theta_n}{d\theta^2} + \lambda_n^2 \Theta_n = 0, \quad (22a)$$

$$\Theta_n(\theta) = \sin(\lambda_n(\theta - \theta_c)), \quad (22b)$$

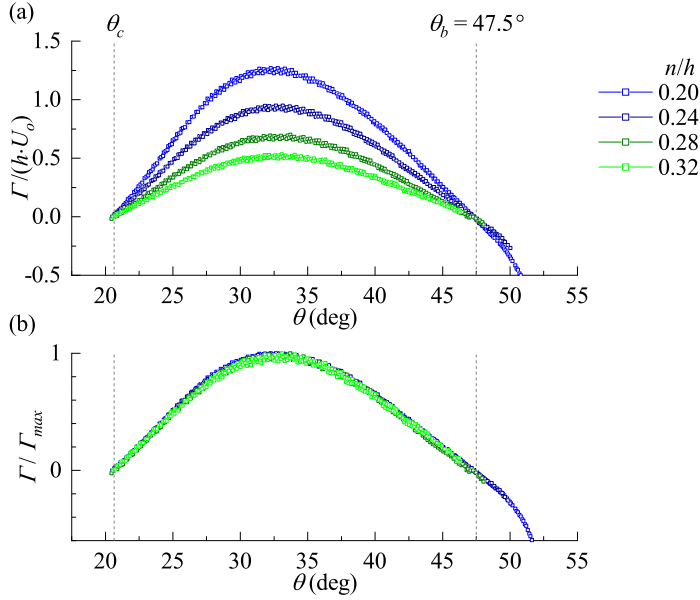


FIG. 12. Circumferential profiles of (a) angular momentum residual and (b) Γ/Γ_{\max} for $\alpha = 90^\circ$ at $D_c/h = 0.7$.

where $\lambda_n = \frac{n\pi}{\varpi}$ by the boundary condition. $R_n(r)$ must satisfy the Cauchy-Euler differential equation described by Eq. (23a) and is of the form shown in Eq. (23b):

$$r^2 \frac{d^2 R_n}{dr^2} + r \frac{dR_n}{dr} - \lambda_n^2 R_n(r) = 0, \quad (23a)$$

$$R_n(r) = \frac{1}{\sqrt{r}} \left(a_n r^{\sqrt{\frac{1}{4} + \lambda_n^2}} + b_n r^{-\sqrt{\frac{1}{4} + \lambda_n^2}} \right). \quad (23b)$$

In Eq. (23b), a_n must be zero since $R_n(r)$ goes to zero for large enough values of r . Now by Eqs. (19), (22b), and (23b), we have

$$L(r, \theta) = A\theta + B + \sum_{n=1}^{\infty} b_n \frac{r^{-\sqrt{\frac{1}{4} + \left(\frac{n\pi}{\varpi}\right)^2}}}{\sqrt{r}} \sin\left(\frac{n\pi}{\varpi}(\theta - \theta_c)\right). \quad (24a)$$

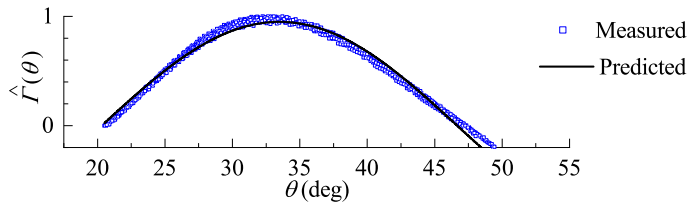


FIG. 13. Plot of the predicted and measured Γ/Γ_{\max} for $\alpha = 90^\circ$ at $D_c/h = 0.7$.

Equation (24a) characterizes the mean angular momentum above the recirculation zone. For completeness, we also present the distribution of the mean velocities below, which may be obtained by solving Eq. (24a) together with Eqs. (5), (8a), and (8b) similarly to the previous cases:

$$U_\theta = \frac{A\theta + B}{r} + \sum_{n=1}^{\infty} b_n \frac{r^{-\sqrt{\frac{1}{4} + (\frac{n\pi}{\omega})^2}}}{r\sqrt{r}} \sin\left(\frac{n\pi}{\omega}(\theta - \theta_c)\right), \quad (25a)$$

$$V_r = \frac{-A \ln r + C}{r} + \sum_{n=1}^{\infty} b_n \frac{\frac{1}{2} + \sqrt{\frac{1}{4} + (\frac{n\pi}{\omega})^2}}{\frac{n\pi}{\omega}} \frac{r^{-\sqrt{\frac{1}{4} + (\frac{n\pi}{\omega})^2}}}{r\sqrt{r}} \cos\left(\frac{n\pi}{\omega}(\theta - \theta_c)\right). \quad (25b)$$

In Eqs. (25a) and (25b), A and B are constants given by Eq. (18). The coefficient b_n is unknown and must be determined by the boundary condition. Unfortunately, there is no exact lower boundary condition in the radial direction due to the presence of the recirculation bubble. Still, if the recirculation bubble is large enough, we may assume that b_n is negligible for $n \neq 1$, and consequently, the angular momentum residual may be approximated by Eq. (26):

$$\Gamma(r, \theta) = R_1(r) \sin\left(\frac{\pi}{\omega}(\theta - \theta_c)\right) \Rightarrow \hat{\Gamma} = \frac{\Gamma(r, \theta)}{\Gamma_{\max}(r)} = \sin\left(\pi \frac{\theta - \theta_c}{\omega}\right). \quad (26)$$

Hence, for $D_c/h = 0.7$ test cases where the recirculation bubble is significantly large, we may fit Eq. (26) to Γ/Γ_{\max} profiles instead of solving for b_n coefficients. An example of such analysis is shown in Figs. 12 and 13 for $\alpha = 90^\circ$ at $D_c/h = 0.7$. Note that $n = 1$ term is no longer dominant for $D_c/h = 0.4$ and 0.2 test cases, and consequently, additional terms must be evaluated according to Eq. (24a).

Levenberg-Marquardt iteration algorithm was used to fit Eq. (27) below to the experimental data, where a coefficient of determination of 0.985 was achieved, indicating a good agreement between the fitted and experimental values. The plot of the Eq. (27) fitted values and the measured data is shown in Fig. 13. The obtained fitting parameters are summarized below. As expected, $\hat{\Gamma}_{\max} \approx 1$, $\theta_0 \approx \theta_c$, and $\hat{\omega} \approx \theta_b - \theta_c$.

$$\hat{\Gamma} = \hat{\Gamma}_{\max} \sin\left(\pi \frac{\theta - \theta_0}{\hat{\omega}}\right), \quad \hat{\Gamma}_{\max} = 0.950, \quad \theta_0 = 20.301^\circ, \quad \hat{\omega} = 26.366^\circ. \quad (27)$$

C. Correlation coefficient

The correlation coefficient is defined by Eq. (28) as

$$\varphi_{u'_\theta v'_r} = \frac{\overline{u'_\theta v'_r}}{\sqrt{\overline{u'_\theta u'_\theta}} \sqrt{\overline{v'_r v'_r}}}. \quad (28)$$

The circumferential evolution of the radial profiles of the correlation coefficient for $\alpha = 45^\circ$ at $D_c/h = 0.7$ is presented in Fig. 14. Within the irrotational region, the correlation coefficient is invariant in the radial direction at a far enough distance from the wall before suddenly decreasing near the edge of the rigid-body rotation region. Note that the correlation coefficient is negative within the rigid-body rotation region. As was observed in Fig. 8, the mean velocity and angular momentum profiles, from the wall to the edge of the rigid-body rotation region, are similar to those of a wall jet over a convex surface. A constant correlation coefficient characterizes a local equilibrium state of turbulent structures [32,33]. Alcaraz *et al.* [32] and Dakos *et al.* [34] reported a correlation coefficient of 0.45 and 0.48 for wall jets over circular cylinders, respectively[33]. Rew and Park [33] reported a correlation coefficient of 0.5 for a circular cylinder of radius of 0.20 m. They attributed the increase in the correlation coefficient to the circular cylinder radius, which was an order of magnitude smaller compared to the previously investigated values. In the present study, for $\alpha = 45^\circ$ at $D_c/h = 0.7$, the correlation coefficient varied between 0.57 to 0.62 in the circumferential direction.

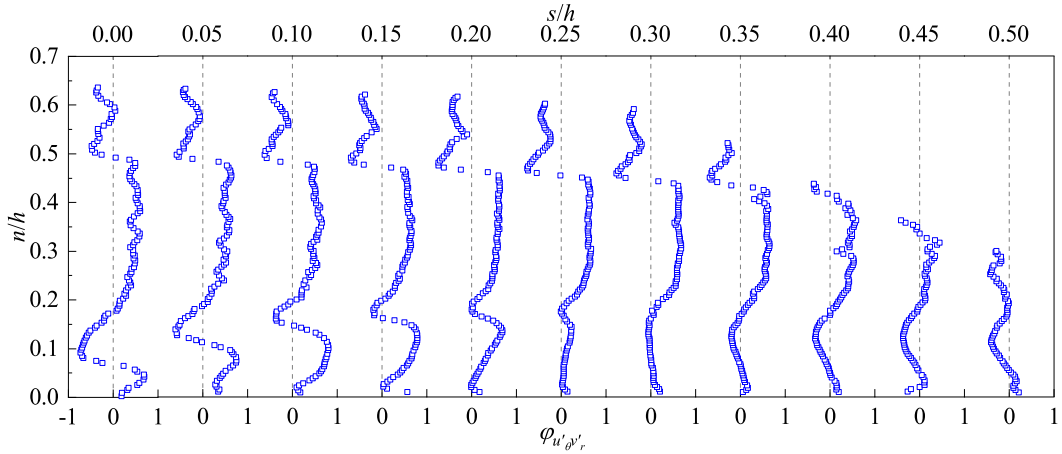


FIG. 14. Circumferential evolution of the radial profiles of the correlation coefficient for $\alpha = 45^\circ$ at $D_c/h = 0.7$.

V. SUMMARY AND CONCLUSIONS

Turbulent flows over circular cylindrical segments with different upstream face angles, namely $\alpha = 90^\circ$, 45° , and 30° , were investigated for three water depths, $D_c/h = 0.7$, 0.4 , and 0.2 , using a double-frame particle image velocimetry system. The height, span-wise extent, and the crest angle of the weir were fixed at 0.15 m, 0.60 m, and 20.6° , respectively. Radial and circumferential profiles of the time-averaged quantities, including the mean span-wise vorticity, mean angular momentum, and correlation coefficient, were investigated to characterize the flow.

Radial profiles of the mean span-wise vorticity revealed several regions that may not be considered irrotational. Two highly turbulent regions were identified along the weir and the free surface. A rigid-body rotation and an irrotational region extended between the two turbulent regions, with the rigid-body rotation region being closer to the free surface. The two highly turbulent regions spread in the circumferential direction and filled the entire flow cross-sectional area for all $D_c/h = 0.2$ test cases and for $\alpha = 90^\circ$ at $D_c/h = 0.4$. The entrance length significantly decreased as the water depth decreased. The rigid-body rotation region extended upstream of the weir crest to $\theta = 0$ for all test cases. Circumferential profiles of the mean span-wise vorticity showed that the vorticity increases in the circumferential direction and then decreases for all test cases within the rigid-body rotation region.

Radial profiles of the mean angular momentum were examined for $\alpha = 30^\circ$ at $D_c/h = 0.4$, where it was observed that the mean angular momentum is invariant in the radial direction within the irrotational region after the reattachment of the flow. It was analytically showed that the mean angular momentum must vary linearly in the circumferential direction if the mean angular momentum is to be invariant in the radial direction. These deductions were confirmed by the circumferential profiles of the mean angular momentum, where it was revealed that the profiles vary linearly and almost collapse on the same line after the reattachment of the flow. It was observed that the mean angular momentum is a constant at the crest for all test cases. Above the recirculation bubble, the profiles diverged before converging to a second intersection point. The line connecting the two intersection points was subtracted from the mean angular momentum profiles and the residual was solved analytically using separation of variables. It was concluded that the residual profiles divided by their maximum collapse on the same curve for $D_c/h = 0.7$ test cases.

Radial profiles of the correlation coefficient were evaluated for $\alpha = 45^\circ$ at $D_c/h = 0.7$. The correlation coefficient was invariant in the radial direction at a far enough distance from the wall within the irrotational region. The measured correlation coefficient was higher than the reported

values in the previous studies on curved wall-jet flows and ranged between 0.57 and 0.62 in the circumferential direction.

The data that support the findings of this study are available from the corresponding author upon reasonable request.

ACKNOWLEDGMENTS

The authors are grateful to the Department of Fisheries and Oceans (DFO) Canada under Contract No. 4500017883 and Canada Foundation for Innovation (CFI) under Project No. 32999 for all forms of financial support and for supplying the experimental facility. The authors would also like to acknowledge the essential technical support provided by Mr. Brendan Pachal.

APPENDIX: TRANSFORMATION OF THE MEAN VELOCITIES AND REYNOLDS STRESSES

The mean velocities in the polar-cylindrical coordinate system were obtained by transforming the Cartesian velocities through Eqs. (A1a) and (A1b):

$$U_\theta = U \cos(\theta) - V \sin(\theta), \quad (\text{A1a})$$

$$V_r = U \sin(\theta) + V \cos(\theta). \quad (\text{A1b})$$

The transformation of the Reynolds stresses was achieved using Eqs. (A2a), (A2b), and (A2c) as

$$\overline{u'_\theta u'_\theta} = \overline{u'u'} \cos^2(\theta) + \overline{v'v'} \sin^2(\theta) - \overline{u'v'} \sin(2\theta), \quad (\text{A2a})$$

$$\overline{v'_r v'_r} = \overline{u'u'} \sin^2(\theta) + \overline{v'v'} \cos^2(\theta) + \overline{u'v'} \sin(2\theta), \quad (\text{A2b})$$

$$\overline{u'_\theta v'_r} = \overline{u'v'} \cos(2\theta) + \left(\frac{\overline{u'u'} - \overline{v'v'}}{2} \right) \sin(2\theta). \quad (\text{A2c})$$

-
- [1] R. B. Jansen, Dams, dikes, and levees, in *Encyclopedia of Physical Science and Technology (Third Edition)*, edited by R. A. Meyers (Academic Press, New York, 2003), pp. 171–190.
- [2] A. H. Azimi, N. Rajaratnam, and D. Z. Zhu, A note on sharp-crested weirs and weirs of finite crest length, *Can. J. Civ. Eng.* **39**, 1234 (2012).
- [3] P. K. Swamee, Generalized rectangular weir equations, *J. Hydraul. Eng.* **114**, 945 (1988).
- [4] A. S. Ramamurthy, N.-D. Vo, and G. Vera, Momentum model of flow past weir, *J. Irrig. Drain Eng.* **118**, 988 (1992).
- [5] L. Schmocker, B. R. Halldórsdóttir, and W. H. Hager, Effect of weir face angles on circular-crested weir flow, *J. Hydraul. Eng.* **137**, 637 (2011).
- [6] A. H. Haghiabi, J. Mohammadzadeh-Habili, and A. Parsaie, Development of an evaluation method for velocity distribution over cylindrical weirs using doublet concept, *Flow Meas. Instrum.* **61**, 79 (2018).
- [7] B. Naghavi, K. Esmaili, J. Yazdi, and F. K. Vahid, An experimental and numerical study on hydraulic characteristics and theoretical equations of circular weirs, *Can. J. Civ. Eng.* **38**, 1327 (2011).
- [8] L. Chunrong, H. Aode, and M. Wenju, Numerical and experimental investigation of flow over a semi-circular weir, *Acta Mech. Sin.* **18**, 594 (2002).
- [9] A. Koch and M. Carstanjen, *Von der Bewegung des Wassers und den dabei auftretenden Kräften: Grundlagen zu einer praktischen Hydrodynamik für Bauingenieure* (Springer, Berlin, Heidelberg, 1926).
- [10] G. D. Matthew, On the influence of curvature, surface tension and viscosity on flow over round-crested weirs, *Proc. Inst. Civ. Eng.* **25**, 511 (1963).
- [11] J. J. Cassidy, Irrotational flow over spillways of finite height, *Journal of the Engineering Mechanics Division* **91**, 155 (1965).
- [12] E. J. Sarginson, The influence of surface tension on weir flow, *J. Hydraul. Res.* **10**, 431 (1972).

- [13] A. S. Ramamurthy and N.-D. Vo, Characteristics of circular-crested weir, *J. Hydraul. Eng.* **119**, 1055 (1993).
- [14] A. S. Ramamurthy, N.-D. Vo, and R. Balachandar, A Note on Irrotational Curvilinear Flow Past a Weir, *J. Fluids Eng.* **116**, 378 (1994).
- [15] H. Chanson and J. S. Montes, Overflow characteristics of circular weirs: Effects of inflow conditions, *J. Irrig. Drain. Eng.* **124**, 152 (1998).
- [16] R. F. Dressler, New nonlinear shallow-flow equations with curvature, *J. Hydraul. Res.* **16**, 205 (1978).
- [17] A. S. Ramamurthy and N.-D. Vo, Application of dressler theory to weir flow, *J. Appl. Mech.* **60**, 163 (1993).
- [18] M. Heidarpour and M. Chamani, Velocity distribution over cylindrical weirs, *J. Hydraul. Res.* **44**, 708 (2006).
- [19] O. Castro-Orgaz, Potential flow solution for open-channel flows and weir-crest overflow, *J. Irrig. Drain. Eng.* **139**, 551 (2013).
- [20] M. Heidarpour, J. M. Habili, and A. H. Haghiabi, Application of potential flow to circular-crested weir, *J. Hydraul. Res.* **46**, 699 (2008).
- [21] N. S. L. Rao, *Theory of Weirs*, edited by V. T. Chow, Advances in Hydrosience, Vol. 10 (Elsevier, 1975), pp. 309–406.
- [22] M. Bos, I. I. Land, and R. Improvement, *Discharge Measurement Structures: Third revised edition*, ILRI publication (ILRI, 1989).
- [23] O. Reynolds, On the dynamical theory of incompressible viscous fluids and the determination of the criterion, *Proc. R. Soc. London. Ser. A* **186**, 123 (1895).
- [24] M. Raffel, C. E. Willert, S. T. Wereley, and J. Kompenhans, *Particle Image Velocimetry: A Practical Guide*, 2nd ed. (Springer Berlin, Heidelberg, 2007).
- [25] M. Samimy and S. Lele, Motion of particles with inertia in a compressible free shear layer, *Phys. Fluids* **3**, 1915 (1991).
- [26] K. Hormann and A. Agathos, The point in polygon problem for arbitrary polygons, *Comput. Geom. Theory Appl.* **20**, 131 (2001).
- [27] A. Sciacchitano and B. Wieneke, Piv uncertainty propagation, *Meas. Sci. Technol.* **27**, 084006 (2016).
- [28] J. S. Bendat and A. G. Piersol, *Random Data: Analysis and Measurement Procedures*, 4th ed. (John Wiley & Sons, 2010).
- [29] H. Chanson, *Hydraulics of Open Channel Flow* (Elsevier, 2004).
- [30] J. Lai and D. Lu, Effect of wall inclination on the mean flow and turbulence characteristics in a two-dimensional wall jet, *Int. J. Heat Fluid Flow* **17**, 377 (1996).
- [31] I. G. Currie, *Fundamental Mechanics of Fluids* (CRC press, 2016).
- [32] E. Alcaraz, G. Charnay, and J. Mathieu, Measurements in a wall jet over a convex surface, *Phys. Fluids* **20**, 203 (1977).
- [33] H. Rew and S. O. Park, The curved wall jet over a circular cylinder before the interaction of two opposing curved wall jets, *KSME Journal* **10**, 86 (1996).
- [34] T. Dakos, C. Verriopoulos, and M. Gibson, Turbulent flow with heat transfer in plane and curved wall jets, *J. Fluid Mech.* **145**, 339 (1984).